Dynamic Response of the Airliner Tail Structure During UAS Airborne Collision

Xianghao Meng[a], Yingjun Sun[b], Jingyu Yu[a,c], Zhongbin Tang[a], Jun Liu[a], TaoSuo[a], Yulong Li[a,*]
[a]*School of Aeronautics, Northwestern Polytechnical University, Xi'an, 710072, China*

[b]*Shanghai Aircraft Airworthiness Certi_cation Center of CAAC, Shanghai, 200335, China*

[c]*Airworthiness Certi_cation Center of CAAC, Beijing, 100102, China*

**Corresponding author. E-mail address: liyulong@nwpu.edu.cn*

An airborne collision between civil Unmanned Aerial Systems (UASs) and manned aircraft is a potential threat to the aircraft operation safety. In this paper, a structure level UAS collision ground test was performed on a commercial airliner horizontal stabilizer section to investigate the dynamic response of this primary operation component. The projectile was a 3.4 kg quadcopter named 'Inspire I'. Explicit dynamic code PAM-CRASH was employed to simulate the collision process and the modeling procedures were modified through comparison with test data. The results showed that 3.4 kg drone impact at the airliner cruising speed could cause some damage on the horizontal stabilizer front spar and the situation is more serious than 3.6 kg bird strike in which the hardness of drone components rather than kinetic energy is a decisive factor. The lithium-ion battery penetrated into the airframe had a smoke sign in the test, which might be a potential ignition source.

I. Nomenclature

E	=	Young's modulus
G	=	Shear modulus
ρ	=	Density
υ	=	Poisson's ratio
σ_y	=	Yield stress
ε_{fail}	=	Failure strain
A,B,n,C,m	=	Material constants in Johnson-Cook mode
T_r	=	Room temperature
T_m	=	Melting temperature
σ_{ij}	=	Stress tensor
ε_{ij}	=	Strain tensor
$\dot{\varepsilon}_{ref}$	=	Reference strain rate
$\varepsilon_i^f, \varepsilon_u^f$	=	Initial/ ultimate longitudinal fiber tensile damage threshold strain
d_u^f	=	Allowed ultimate fiber damage
d,d'	=	Scalar shear/transverse damage factor
Y_0,Y_c	=	Initial/critical shear damage value
Y'_0,Y'_c	=	Initial/critical transverse damage value
T_{max}	=	Maximum tensile force
S_{max}	=	Maximum shear force
D_1	=	Energy absorption distance after failure
D_2	=	Ultimate failure distance
P_0	=	Initial pressure in Murnaghan EOS
ρ_0	=	Initial density in Murnaghan EOS
B, γ	=	Material constants in Murnaghan EOS

II. Introduction

Aircraft structures are vulnerable to impacts from foreign objects such as debris, hails or bird strike. These impact incidents are serious threats to the operation safety of civil aircraft and may cause catastrophic accidents. According to FAA's reports [1], more than 245 aircraft and 258 people were lost in wildlife strike incidents since 1990. Nowadays, the explosive growth in civil UASs makes the impact scenarios even more complicated. The Association for Unmanned Vehicles Systems International (AUVSI) forecasted that the UAS market volume would reach 4.7 million units by 2020 [2]. UP to now, at least 28 collision or near collision incidents between UASs and trunk liners have been reported since 2014, the number of which increased year by year.

Concerns about UAS operation safety issues have continued for more than ten years. Up to now, much interest has been directed to the collision avoidance algorithms [3,4] or collision avoidance systems [5]. Although these methods may to some extent reduce the risk of accidental collision incidents but seem to be useless to those malicious ones. Damage assessment is still a crucial part of airworthiness certification.

UAS collision ground tests provide a direct method to evaluate the damage severity. But the high cost of test procedures makes it's challenging to enumerate all collision scenarios. With the rapid development of finite element method (FEM), combined experimental and numerical methodology was proved to be an efficient way to improve the design safety while significantly reduce certification costs, as pointed out by Georgiadis [6]. According to FAR 25.631, a bird strike test can be replaced with an appropriate numerical analysis as long as the results have been validated against a representative aircraft structure [7]. We think the same methodology could also be used on the damage assessment of UAS airborne collision.

Civil Aviation Safety Authority [8] investigated the damage potential of UAS airborne collision on the engine ingestion, fuselage, and cockpit windshield and made a rough estimate of the penetration velocity. The Department for Transport, the Military Aviation Authority and the British Airline Pilots' Association [9] performed a UAS collision ground test to investigate the hazard to the windshield. During the test, drones were dismantled and launched by a gas gun, which could hardly reflect real collision scenarios and the correlation between simulation and experiment was not satisfactory. Song et al [10,11] investigated the dynamic response of a high-bypass engine during drone ingestion, different risk levels were classified and a comparison with bird ingestion was performed. Recently, FAA reported the quadcopter [12] and fixed-wing [13] UAS airborne collision severity evaluation. In which a series of component level tests were performed to calibrate the numerical model and damage severity of different collision scenarios on commercial transport jet and the business jet was evaluated. It was concluded that UAS collision could introduce severe damage to aircraft structures. However, the simulation models have not been validated by structure level test data yet.

The horizontal stabilizer is one of the primary operational components of the aircraft, the leading edge of which must be certified for 3.6 kg bird strike resistance. No significant damage should be detected on the front spar (part of the torsion box) and control devices in order to ensure the operation safety. Many researchers introduced novel designs such as aluminum foams filler [14], sandwich structure [7], and triangular reinforcement [15]. However, these reinforcements were mainly targeted at bird strike problems, the threats associated with UAS airborne collision have not been fully considered during civil aircraft design or operation process.

Up to now, almost no structure level test data of UAS collision on horizontal stabilizer leading edges could be found in published reports. In this work, such test was performed, a section of a commercial airliner horizontal stabilizer (already certified for 3.6 kg bird strike) was employed as the target specimen and the projectile was a 3.4 kg drone. The collision simulations were carried out by explicit dynamic finite element solver PAM-CRASH. The simulation model was modified by comparing the morphology and strain signals with test data and showed acceptable agreement. A comparison with bird strike was also clarified in this paper. Based on these results, the threats associated with UAS airborne collisions to the horizontal stabilizer was summarized, which is of certain reference value on the security risk assessment of civil aircraft under UAS airborne collision.

III. Description of the FE model

A. The Drone

'Inspire I' professional supplied by SZ DJI Technology Co., Ltd. was selected to be the representative quadcopter in the test. Its general size was about 410*440*330 mm and the total weight (with camera) was 3.428 kg, which was close to the bird mass required by the bird strike resistance certification for tail leading edges (3.6 kg). Reverse engineering method was applied to generate the drone FE model, the drone was dismantled and the sizes of components were obtained through manual measurements. Some minor components and geometric features were eliminated, their mass was added to the main structure to keep the total mass and center of gravity unchanged. Shell elements were used to represent thin-walled structures such as the fairing and brackets, solid elements were used to represent the battery, motors, and camera. Although these components had their own internal structures, they were treated as homogeneous entities to simplify the simulation model. Based on a mesh sensitivity study in Section 2.5, the average element size was about 4-5 mm and shown in Fig. 1c, for some minor components, smaller mesh size was employed based on their geometric features. The drone model contained 22,971 shell elements and 11,544 solid elements. The materials and mass distribution are shown in Fig. 1a and b.

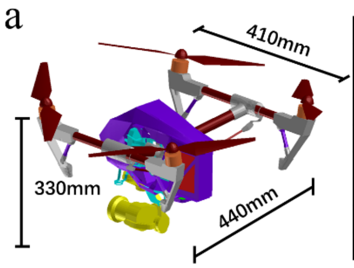

Code	Material
	Polycarbonate
	Polyamide 6
	Carbon Fiber Reinforced Polymer
	battery
	camera
	6061-T6 aluminum alloy
	electronic boards
	motor

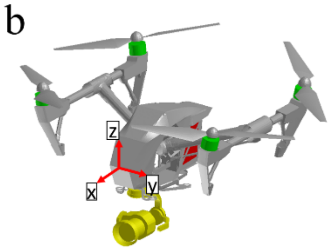

Component		Mass/kg	Center of gravity/mm
Total UAS		3.428	(-197, 0, 5)
	motors	0.462	(-214, 0, 12)
	battery	0.57	(-271, 0, 4)
	camera	0.64	(-125, 0, -161)

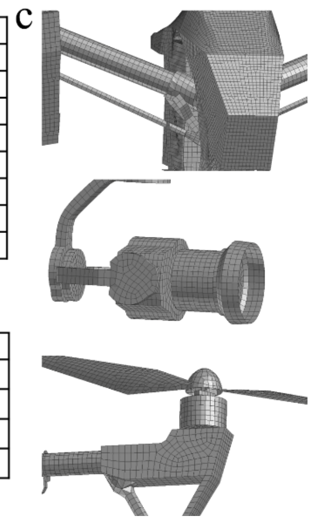

Fig. 1 a) Drone materials b) mass distribution c) element size

B. Horizontal stabilizer leading edge

A commercial airliner horizontal stabilizer leading edge segment was prepared for the test. The segment was about 1 m in length and the total mass was 9.96 kg. It consisted of a skin, a triangular reinforcement, seven ribs, and a front spar, as shown in Fig. 2a. Notice that the triangular reinforcement was a novel anti-bird strike design introduced by Liu et al [15], as can be seen from Fig. 2b that during the bird strike process, the skin would deform along the reinforcement and form a knife-like a shape, the bird would be cut into two parts and slid away from the leading edge, which could mitigate impact loading and provide better protection for the front spar. The triangular reinforcement was manufactured by bending two layers of 1 mm 7075-T6 aluminum alloy to an open angle of 85 ° with a curvature less than 5 mm, then fix them on ribs by connectors.

The leading edge specimen was fixed on a Q235 steel fixture and then mounted on the rocket sled. To obtain a balanced aerodynamic load, the specimen was set to be perpendicular to the impact direction (no swept angle). Two semi-oval Q235 fixtures were fixed on two sides of the specimen to restrict displacement along impact direction. Both the leading edge and fixture were represented by shell elements, through a mesh sensitivity study in Section 2.5, an average mesh size of 5 mm was employed for the leading edge and fixture mesh size was about 15 mm. The whole model contained 84,124 shell elements.

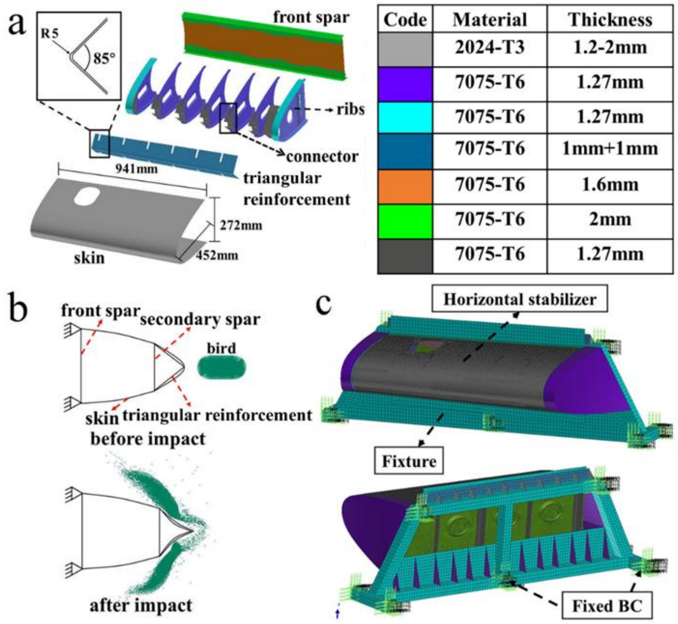

Fig. 2 a) Geometric details and materials of the leading edge specimen. b) Schematic of the triangular reinforcement. c) Fixture and boundary conditions.

C. Constitutive model for materials

The aluminum alloy 2024-T3, 7075-T6, and 6061-T6 were represented by the elastic-plastic material with isotropic damage model, the flow stress and strain rate dependent behavior were described by Johnson-Cook's law [16], the expression is:

$$\sigma = (A + B\varepsilon^n)(1 + C\ln\dot{\varepsilon}^*)(1 - (T^*)^m) \tag{1}$$

And

$$T^* = (T - T_r)/(T_m - T_r) \tag{2}$$

During the collision process, most of the material failure was due to tensile stretching caused by the displacement of the impact region [15]. Therefore, the maximum tensile strain value was employed as the mesh elimination criterion. All these parameters were obtained through static tests on electromechanical load frames and dynamic tests on Split Hopkinson Bars (SHBs) and are listed in Table 1. Notice that we did not measure the temperature rising and only used the first and second term of J-C model. The Q235 steel was represented by a linear elastic model without failure, where E = 200 GPa and μ = 0.3.

Table 1. Parameters of aluminum alloy

	A [MPa]	B [MPa]	n	C	$\varepsilon_{\max}$
2024-T3	280	400	0.2	0.015	0.2
7075-T6	480	400	0.42	-0.001	0.12
6061-T6	324	114	0.42	0.002	0.12

The CFRP material was represented by a PAM-CRASH built-in unidirectional composite global ply model based on ref [17]. It corresponded to a homogenized, global description of the fiber and matrix phases. Three global composite ply damage phenomena were considered: matrix microcracking, fiber/matrix debonding and fiber rupture. The elastic stress-strain relation is formulated below:

$$\begin{Bmatrix} \varepsilon_{11} \\ \varepsilon_{22} \\ 2\varepsilon_{12} \\ 2\varepsilon_{23} \\ 2\varepsilon_{13} \end{Bmatrix} = \begin{pmatrix} 1/E_1 & -\nu_{12}/E_1 & 0 & 0 & 0 \\ -\nu_{12}/E_1 & 1/E_2 & 0 & 0 & 0 \\ 0 & 0 & 1/G_{12} & 0 & 0 \\ 0 & 0 & 0 & 1/G_{23} & 0 \\ 0 & 0 & 0 & 0 & 1/G_{12} \end{pmatrix} \begin{Bmatrix} \sigma_{11} \\ \sigma_{22} \\ \sigma_{12} \\ \sigma_{23} \\ \sigma_{13} \end{Bmatrix} \tag{3}$$

Some basic elastic parameters are listed in Table 2. For fiber tensile damage, the damaged Young's modulus E_1 was calculated by:

$$E_1 = \begin{cases} E_1^0 & \varepsilon_{11} < \varepsilon_i^f \\ E_1^0(1-d^f); \quad d^f = d_u^f \dfrac{\varepsilon_{11}-\varepsilon_i^f}{\varepsilon_u^f - \varepsilon_i^f} & \varepsilon_i^f \le \varepsilon_{11} < \varepsilon_u^f \\ E_1^0(1-d^f); \quad d^f = 1-(1-d_u^f)\dfrac{\varepsilon_{11}}{\varepsilon_u^f} & \varepsilon_u^f \le \varepsilon_{11} \end{cases} \tag{4}$$

Where $\varepsilon_i^f = 0.019$, $\varepsilon_u^f = 0.023$, and $d_u^f = 0.99$ was employed in this paper, reflected a brittle fracture for the fiber. The parameters were measured by tensile loading in the fiber direction.

Two scalar variables, *d* and *d'* were employed to quantify the matrix related damages. *d* was related to the damage due to debonding between fibers and matrix, and *d'* was related to the matrix microcracking parallel to the fiber direction. The damage evolution functions are defined as below:

$$\begin{cases} Y = \sqrt{\dfrac{1}{2}\dfrac{\sigma_{12}^2+\sigma_{13}^2}{G_{12}} + b\dfrac{1}{2}\dfrac{\langle \sigma_{22} \rangle^2}{E_2}} & \text{(shear damage)} \\ Y' = \sqrt{\dfrac{1}{2}\dfrac{\langle \sigma_{22} \rangle^2}{E_2}} & \text{(transverse damage)} \end{cases} \tag{5}$$

Where <a>=a if a>0, else=0. (because the microcracks grow when the composite ply was under tensile transverse loading and close under compression) *b* was the coupling factor between shear and transverse damage (default value=E_2/G_{12}). The damage scaler *d* and *d'* were calculated from:

$$\begin{cases} d = \langle Y - Y_0 \rangle / Y_c & \text{(shear damage)} \\ d' = \langle Y - Y'_0 \rangle / Y'_c & \text{(transverse damage)} \end{cases} \tag{6}$$

Where $Y_0 = 0.345\sqrt{MPa}$, $Y_c = 3.42\sqrt{MPa}$, $Y'_0 = 0.282\sqrt{MPa}$, and $Y'_c = 6.79\sqrt{MPa}$ These parameters were measured by loop loading. The damaged Young's modulus E_2 and shear modulus G_{12} thus can be calculated by:

$$\begin{cases} E_2 = E_2^0(1-d') \\ G_{12} = G_{12}^0(1-d) \end{cases} \tag{7}$$

A mesh elimination criterion based on the maximum shear strain (5%) was employed to avoid large mesh distortion associated with stiffness degradation.

Table 2. Elastic parameters of CFRP

Young's modulus E_1 [GPa]	Young's modulus E_2 [GPa]	Poisson's ratio ν_{12}	Shear modulus G_{12}[GPa]
191	9.9	0.33	63

The polycarbonate (PC) and polyamide6 (PA6) material were represented by the elastic-plastic model and were assumed to be ideal plasticity. The mechanical properties were supported by SZ DJI Technology Co., Ltd and are listed in Table 3. The maximum tensile plastic strain was set to be the criterion for element elimination and the parameters were modified through comparison with test data. Different values ranged from 0.1 to 0.4 at an interval of 0.05 were tested and finally, the value 0.2 was employed in the simulation.

Table 3. Parameters of PC and PA6

	Density ρ [kg/m^3]	Young modulus E [GPa]	Poisson's ratio ν	Yield stress σ_y [MPa]	Failure strain ε_{max}
PC	1180	2.35	0.3	62	0.2
PA6	1350	6.2	0.3	70	0.2

Sahraei et al [18,19] studied the mechanical properties of pouch lithium-ion batteries, and a 60% porosity of the active particles with the voids filled with electrolyte was estimated by them. So they used a crushable foam element in the first approximation. A similar model was employed in this paper and some basic parameters are listed in Table 4.

Table 4. Mechanical properties of the battery

Density ρ [kg/m^3]	Young modulus E [MPa]	Poisson's ratio ν

1750	500	0.01

D. Joints model

Mesh independent PLINK elements were employed to simulate fastened joints. Penalty stiffness was internally calculated to achieve a stable response. A user-defined rupture model is expressed as follow:

$$\left(\frac{T}{T_{MAX}}\right)^n + \left(\frac{S}{S_{MAX}}\right)^m \le 1 \tag{8}$$

T and S mean the tensile force and shear force calculated during the simulation process. Ultimate tensile load T_{MAX} = 3000 N and shear load S_{MAX} = 4200 N for rivet code '4.0-8-CPH' was measured on the SHBs. n = 1.5, m = 2.1 were determined according to ref [20]. To eliminate oscillations in stress, T and S were set to be the average value in thirty integral circles. A displacement-based post failure softening relevant was applied with D_1 = 0.5 mm and D_2 = 1 mm mean the energy absorption distance after failure was initiated and the ultimate failure distance respectively. To avoid local stress concentration induced by PLINK elements, six additional points at a radius of 3 mm were added to every PLINK element. The tail leading edge model contained 753 PLINK elements.

Complicated connection relationship between different drone components makes it difficult to set PLINK elements corresponding to real bolts arrangement. Instead, modified TIED elements with the same rupture model were employed. Since TIED elements were mesh dependent and the rupture parameters were related to mesh size, extensive parametric studies were performed to determine suitable parameters for the impact scenario. The welding connections in the fixture were also represented by TIED elements but no rupture model was considered here.

E. Computational model

A mesh sensitivity study was performed to obtain a balance between accuracy and computational efficiency. To perform the study, some representative drone components, i.e. the battery cell and motor were impacted to an aluminum alloy flat plate (500*500*2 mm, 2024-T3, same as the leading edge external skin) at a velocity of 151 m/s. the mesh sizes of the FE model were 15 mm, 10 mm, 5 mm, 3 mm and 2 mm. The internal energy of the battery cell was employed as the criterion and shown in Fig. 3. It can be seen that the performances of the FE models were almost identical when the mesh size was below 5 mm. The morphology of the plate impacted by the motor also shows that the mesh elimination criterion still worked well when the mesh size increased from 2 mm to 5mm. Finally, an average element size of 5 mm was employed in this work.

The explicit analysis was employed in this simulation. Its effectiveness in solving highly non-linear problems has been reported by many authors. To capture all energy associated with the stress wave propagation during the impact process, the critical time step was around 1.6*10-7 s. The time step required for stability was computed by the program, and the solution was stable with the default time step scale factor (constant value = 0.9).

The contact behavior was represented by a PAM-CRASH built-in 'self-impacting node to segment' contact. This contact type required the definition of one surface (slave) only. Each node/edge of the slave side was checked for penetrations to the segments/edges of the slave side. Penalty method was employed to avoid perforation. The friction behavior between the drone and the leading edge was governed by Coulomb friction law and the constant friction coefficient was set to be 0.26 according to a material handbook. The average contact thickness was set to be 1 mm, and local contact thickness was modified to avoid initial penetration.

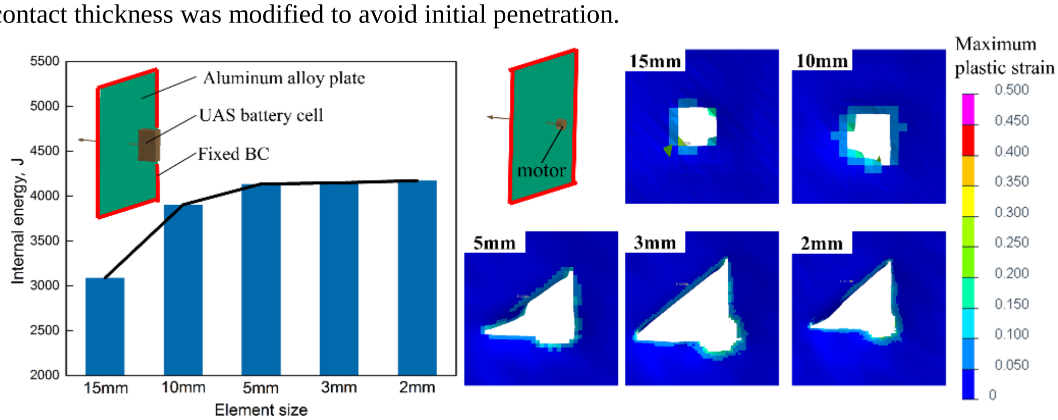

Fig. 3 Mesh sensitivity study

IV.Experimental validation

A. Test collision scenario determination

In this section, a series of simulations were performed to study the effect of different impact locations and drone postures on the dynamic response of the horizontal stabilizer, among which the most serious scenario shall be employed in the UAS collision ground test.

The impact velocity was set to be 151 m/s, this velocity combined the drone's maximum velocity of 25 m/s and airliner velocity of 126 m/s at an altitude of 500 m according to its flight envelope. Two impact locations were investigated, on the rib and between ribs, as shown in Fig. 4a. Fig. 4b shows that the battery cell and some other drone components broke the triangular reinforcement and hit the front spar when the impact location was between two ribs, which was assumed to be more serious than the on rib situation.

Different drone postures were also investigated, while the center of gravity of the drone was kept still. The attack angle varied from -45◦ to 45◦ at an interval of 22.5◦ and the yaw angle varied from 0◦ to 180◦ at an interval of 45◦. The impact scenarios were marked 1#-5# and shown in Fig. 4c and d. The internal energy of the front spar reflected the deformation severity of this primary structure and was employed as the criterion to evaluate the collision consequences. From the results in Fig. 4e, it can be assumed that the drone with no attack angle and no yaw angle would cause the most serious consequence. And this collision scenario shall be employed in the collision test.

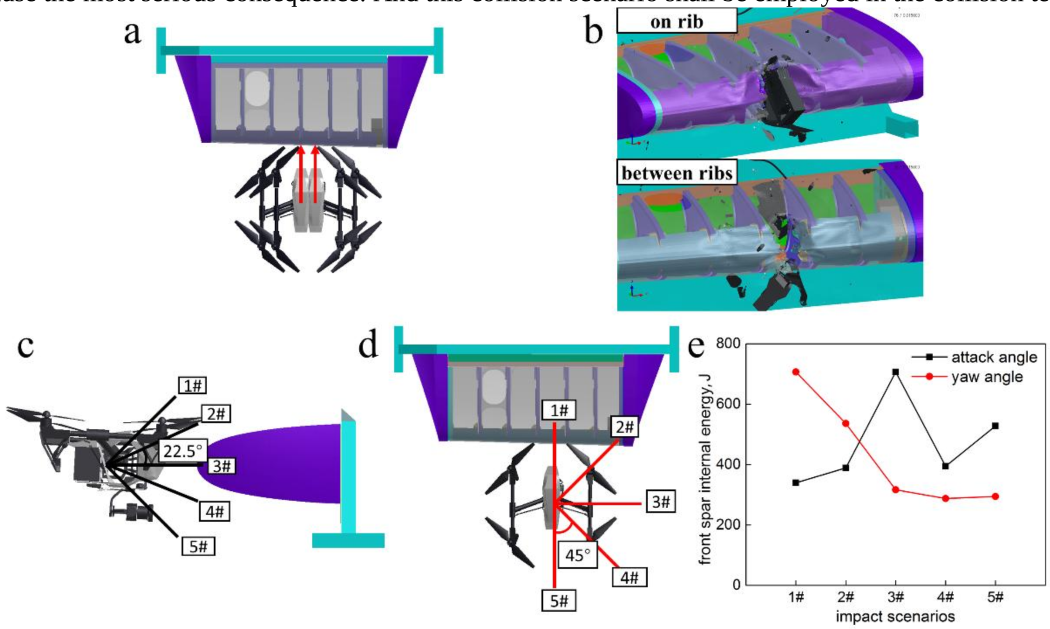

Fig.4 a) Different impact locations and b) damage characteristics. Different c) attack angle and d) yaw angle and e) front spar internal energy

B. Test procedure

The UAS collision ground tests were performed at the experimental base of Aerospace Life-support Industries.,Ltd. Fig. 5. illustrates the arrangement of the test apparatus. The leading edge specimen and aircraft head structure (employed in the windshield collision test) were mounted on a rocket sled. The sled can move freely along the lubricated steel track and the launch point was 300 m from the suspended drone. The fuel in the booster rocket was carefully calculated to provide enough thrust and achieve the expected speed of 151 m/s at the impact point. The actual velocity of the sled was measured through radiotelemetry and shown in Fig. 6. The velocity at the impact point was 152.8 m/s, about 1.2% higher than expected one, then the fuel exhausted and the sled reaches the maximum speed of 159.2 m/s. After that, the sled was slowed down to stop by the friction with track and water brake. Fig. 7a. shows the rocket sled employed in collision ground test.

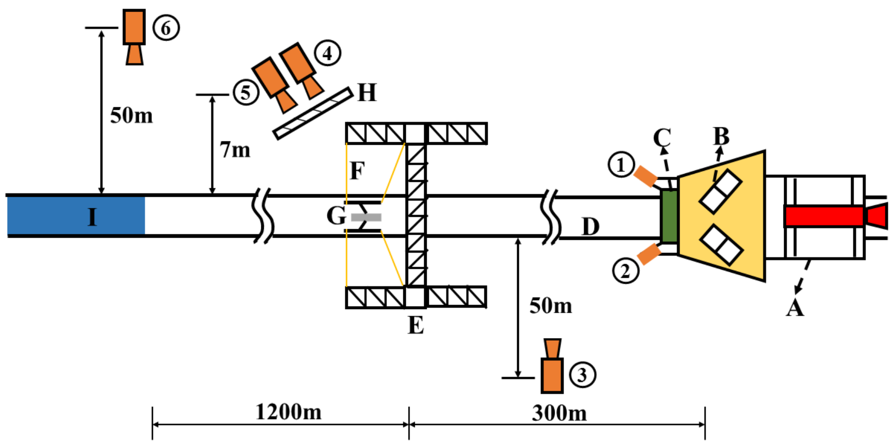

Fig.5 Schematic diagram of the UAS collision test apparatus. (A) rocket sled, (B) head structure and windshield, (C) horizontal stabilizer leading edge, (D) steel track, (E) fixture frame for the drone, (F) KEVLAR strings, (G) the drone, (H) shield for high-speed cameras, (I) water brake. 1-6 high-speed cameras.

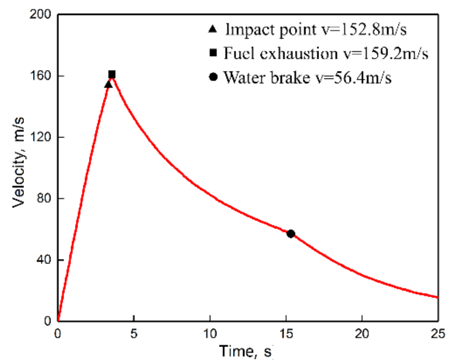

Fig.6 The velocity of the rocket sled

According to the results in Section 3.1, the drone was suspended horizontally with no attack angle and no yaw angle. The motors were set to be energized during the impact process to reproduce real impact scenario and to see whether the impact loading would cause short circuit or explosion of the lithium-ion battery cell. 8 KEVLAR strings were used to suspend the drone at the target impact location, as shown in Fig. 7b. the arrangement of these strings should follow the guidelines below: i) All six degrees of freedom for the drone should be restricted by strings and withstand the turbulent flow caused by rocket sled's movement; ii) No strings should contact with the horizontal stabilizer structure before the drone; iii) All strings should break immediately at the time of impact and have little interference on impact loading and debris trajectory.

Six high-speed cameras were employed in the test, two of them at 3,000 frames per second were fixed on the rocket sled (1 and 2 in Fig. 5) and were protected by aluminum alloy shields from the debris during the test process. Another two cameras (4 and 5 in Fig. 5) at 5,000 frames per second were placed near impact point to monitor the damage characteristics of the leading edge specimen. The frame rate for the cameras was not very high and was just enough to capture the damage caused by some typical drone components. Last two cameras (3 and 6 in Fig. 5) were placed 50 meters away from the track to monitor the movement of rocket sled during the whole test process at 240 frames per second. 11 strain gauges (type BE350-3AA) were arranged on the horizontal stabilizer to record the dynamic strain response of the structure, as shown in Fig. 7c. S1-S5 were arranged on the leading edge ridge line, S6-S9 were arranged on the upper and lower side of the skin, S10-S11 were arranged on the front spar. All these gauges were at least 15cm from the impact point to protect them from the debris of the drone. The oscilloscope at the frequency of 50,000 Hz was also fixed on a rocket sled.

To obtain the accurate aerodynamic characteristics of the rocket sled and verify the data collection system, a preliminary test was performed on the windshield with a 0.3 kg drone, as shown in Fig. 7d. During the test, all high-speed cameras were trigged correctly and captured the whole collision process. Three of the four strain gauges arranged on the windshield had valid data while the weld point of one gauge was broken due to impact loading. The KEVLAR strings (maximum loading was 600 N) used to suspend the drone were too strong and couldn't break immediately at the time of impact (red circles in Fig. 7d.) and they were replaced by KEVLAR string with a maximum loading of 300 N in the formal test.

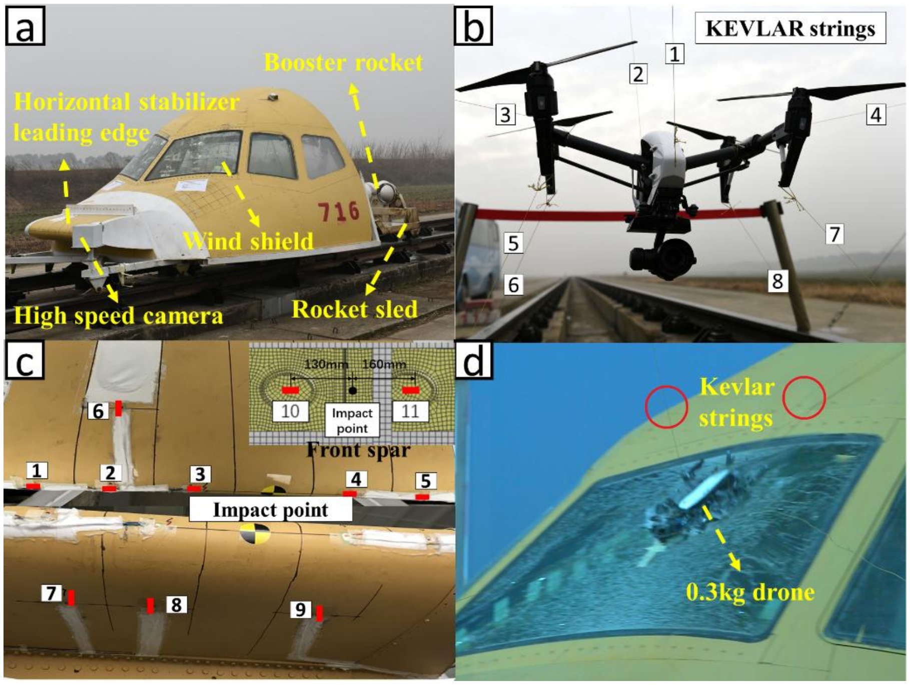

Fig.7 a) Rocket sled used in the UAS collision test. b)The drone suspended by 8 KEVLAR strings. c)Strain gauges on the leading edge specimen. d) A preliminary test on the windshield with a 0.3 kg drone.

C. Comparison between test and simulation results

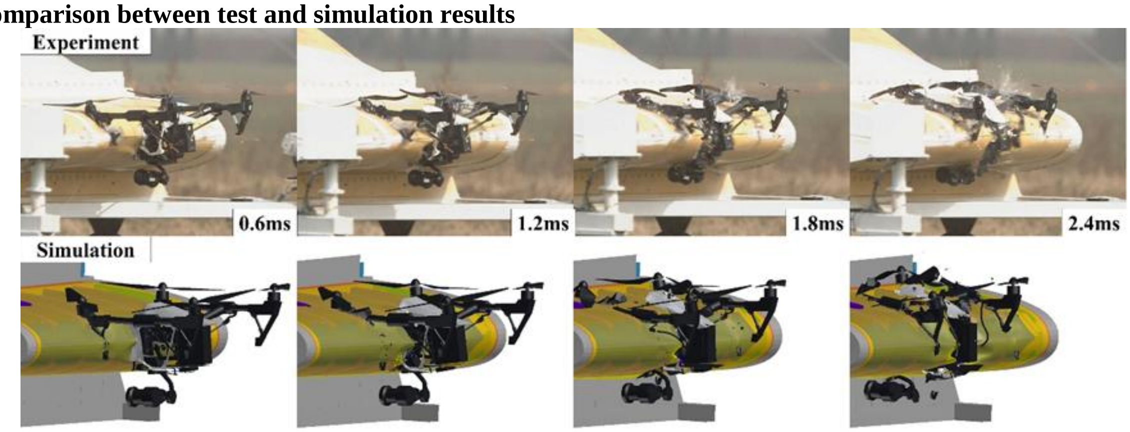

Fig.8 Images from high-speed camera and simulation during the UAS collision test.

During the UAS collision process, the leading edge external skin and triangular reinforcement were fractured and considerable portions of UAS mass (including the lithium-ion battery cell) penetrated into the airframe, while two arms and motors slid away from the upper skin. The bracket of the drone's camera was broken and the camera slid away along the lower skin. The deformation characteristics captured by high-speed cameras were compared with the simulation results at different time intervals in Fig. 8. From the figures, we can assume that the penetration happened about 1.2-1.8 ms after the collision began and the triangular reinforcement seems to be useless against UAS collision. Good agreement between the test and simulation results was achieved in deformation characteristics.

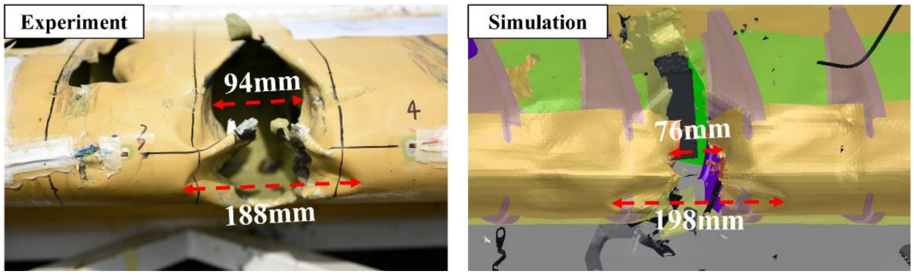

Fig.9 Comparison of damage characteristics on between the test and simulation

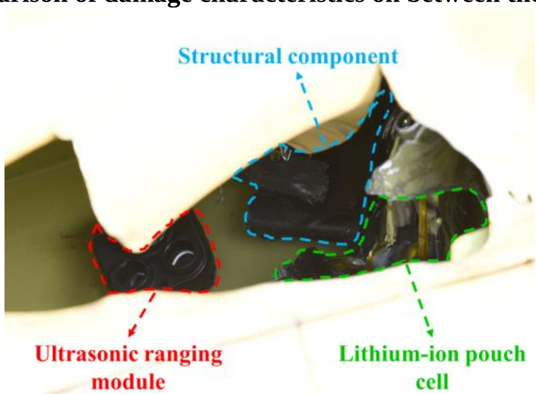

Fig.10 Drone components penetrated into the airframe

Fig. 9. illustrates the damage features of the leading edge specimen after the collision and that from the simulation. the acceptable agreement can be observed in the deformation area (188 mm versus198 mm), but the fracture size from simulation was reasonably smaller than the test (76 mm versus 94 mm). Notice that there was a fracture on the left side of the leading edge, that's probably because the drone tilted to the left during the collision process and the left arm scratched the upper skin. Which was not reflected in the simulation. Fig. 10 shows some drone components penetrated into the airframe, the lithium-ion battery cell was crushed and showed some smoke and charred smell right after the test, which indicated that short circuit probably happened and the cell shall be a potential ignition source.

Fig. 11. shows the comparison between surface strain signals measured by strain gauges on the leading edge specimen and that from the simulation. Six of the eleven gauges get acceptable data while the others failed due to impact loading. The simulation results have some discrepancies with test data, which can be attributed to the randomness factors during the collision process and the differences between the simplified drone FE model and real drone structure. The survived strain gauges were about 30 cm from the impact point and the measured stain singles were less than 0.5%, which indicated that the dynamic response of the leading edge was a local behavior, that is different from bird strike and shall be discussed in Section 5.

According to the airworthiness standards, it can be assumed that at the impact velocity of 151 m/s, primary structure of the horizontal stabilizer would not suffer much, but fire risk of the lithium-ion battery should be considered and the residual strength should be evaluated to ensure the flight safety..

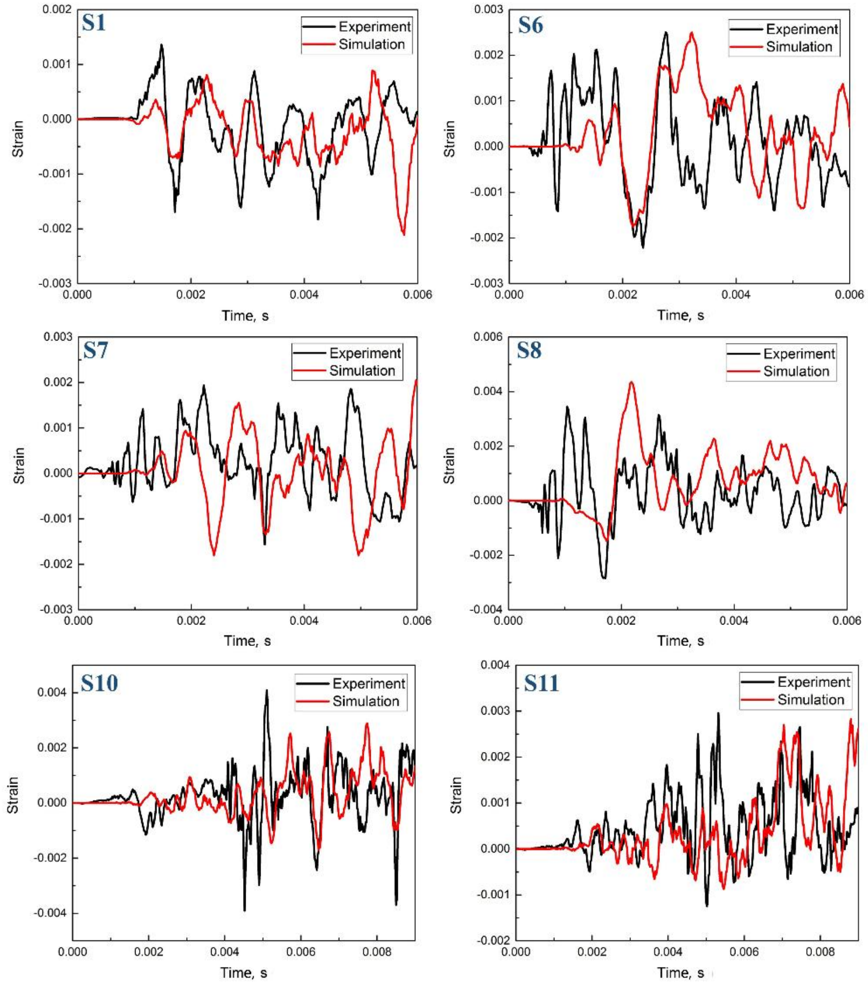

Fig.11 Comparison between measured and simulated strains on horizontal stabilizer leading edge

V.Comparison with bird strike

A. Bird model

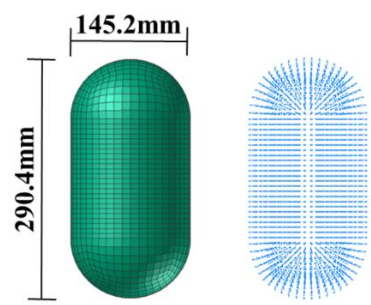

Fig. 12. The SPH bird model

The meshless Smoothed particle hydrodynamics (SPH) model was adopted to simulate the bird. It was developed by Lucy in 1970s to overcome large mesh distortion in high-speed impact problems. This technique used discrete, topologically independent particles instead of solid mesh, the interaction between these particles was controlled by interpolation theory and smoothing kernel functions. Its advantages in stability and accuracy was emphasized in Hemibs's [21] review. The same conclusion was also drawn by Liu et al [22] through comparison between simulation results from Lagrangian and SPH model and test data from bird strike on flat plates. Megiud [23] studied the effect of different bird geometries on impact results through numerical method, and a cylinder with hemispherical ends with a length to diameter ratio of 2:1 was recommended. According to FAR 25, subpart 25.571, a 3.6 kg bird with an average density of 900 kg/m^3 was adopted, the SPH model contained 15,246 particles and is shown in Fig. 12. Notice that this bird model is a homogenized approximation, which do not consider the differences between bird organs such as muscles or bones, and can only be employed to predict the macro response of the structure in bird strike problems.

The equation of state (EOS) described the pressure-volume relationship of materials and is widely used to describe the constitutive relations of fluid-like materials when the flow velocities remain well below the physical volume sound speed. Which is a typical characteristic for bird materials during bird strike process, as pointed out by Welbeck [24]. Guida [25] and Somjver [26] employed different EOSs to study bird strike on aircraft structures and emphasized the importance of selecting suitable EOS for different impact scenarios. In this work, Murnaghan EOS was employed and the expression is:

$$p = p_0 + B\left[\left(\frac{\rho}{\rho_0}\right)^{\gamma} - 1\right] \tag{8}$$

McCarthy [20] performed bird strike tests on flat plates and determined B = 128 MPa and γ=7.99 by inversion of parameters.

B. Results and discussion

The comparison between 3.4 kg UAS collision and 3.6 kg bird strike is shown in Fig. 13a and b. the impact velocity was 151 m/s. During the bird strike process, the triangular reinforcement cut the bird body and the debris slid away from the structure, the skin suffered extensive permanent deformation but no penetration was observed. However, the drone structures broke both the skin and triangular reinforcement and penetrated into the airframe, which may cause damage to the front spar and control devices, according to airworthiness standards, the UAS collision was assumed to be more dangerous. Under the same impact velocity, the kinetic energy of the drone was 95.2% of that of the bird, and the severer impact consequences can be attributed to the following two reasons.

First, the bird material performed fluid like mechanics and would splash during the impact process, which would increase contact area and mitigate impact loading. Under bird strike, an overall deformation of the leading edge external skin can be observed from the strain cloud map. Also, the energy absorbed by the deformation of the airframe was about 56% higher than UAS collision, the bird kinetic energy was dispersed and no penetration happened. However, the drone structure showed solid characteristics during the collision process, the impact loading was more concentrated and caused local deformation and penetration.

Second, Although the bird body contained bones, muscles, and other tissues of different densities, the bird strike on flat plate tests [22] showed that it could still be treated as a homogenous entity in the simulation. However, the drone contained hard blocks such as battery, motors, and camera, which could cause extremely high impact loading and local high-stress areas. As can be seen from the curve in Fig. 16d that the contact force amplitude of UAS collision was much higher than bird strike but the pulse width was rather short. These hard bocks would cause partial perforation of the external skin and finally, lead to large penetration.

From the discussion above, it can be assumed that during the UAS collision process the hardness rather than kinetic energy played the critical role, that is the biggest difference between UAS collision and bird strike.

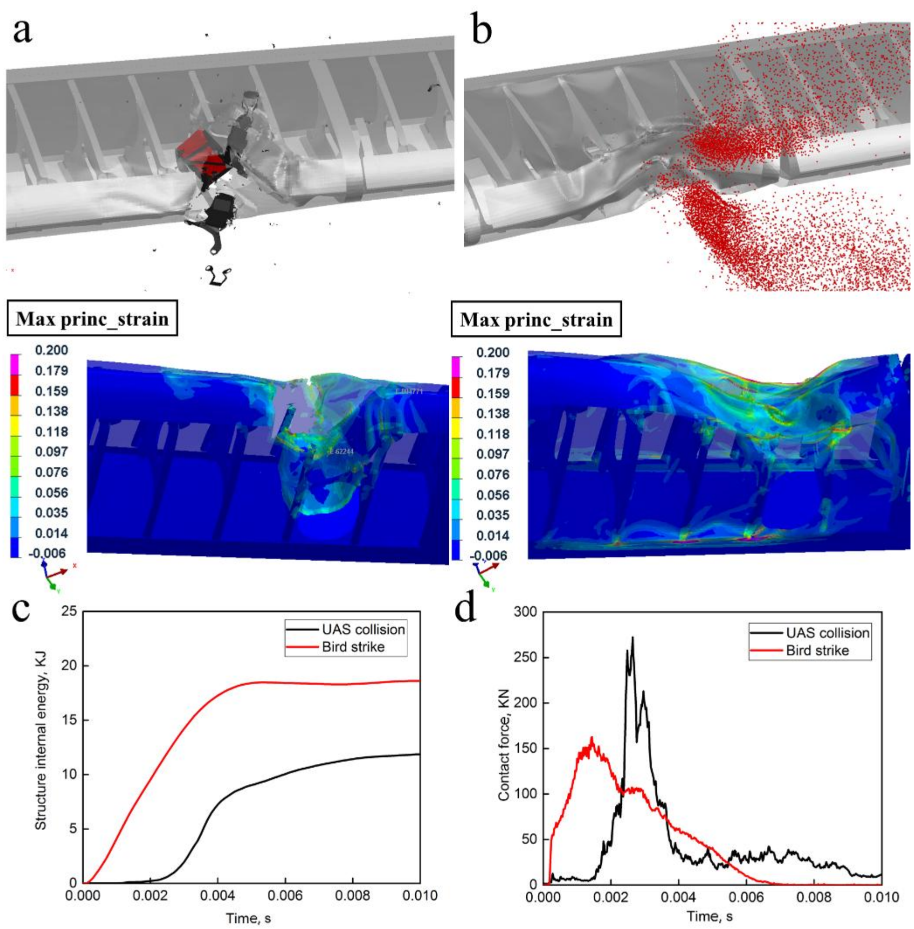

Fig. 13. Damage characteristics of a) UAS collision and b) bird strike. c) Aircraft internal energy and d) contact force during the UAS collision and bird strike process

VI. Conclusion

In this paper, an attempt is made to analyze both experimentally and numerically a UAS collision against aircraft horizontal stabilizer. The numerical framework was developed and validated with experimental data after numerical validation various impact scenarios were simulated to study the risk of UAS impact on different locations of the horizontal stabilizer. The comparison between UAS and bird collision with the subject target was also made. The following conclusions from this study can be drawn:

1) The impact behavior simulated by the FE model developed in this paper was in acceptable agreement with test data and the simulation methodology was proved to be an efficient way to reduce certification costs.

2) The commercial airliner cannot complete the flight safely when a UAS airborne collision happens at its cruising speed, considering the damage to the horizontal stabilizer front spar and fire risk of the lithium-ion battery.

3) Some novel anti-bird strike designs such as triangular reinforcement were proved to be not so efficient against UAS airborne collision, and new design principles should be considered.

4) UAS collision would cause more serious consequences than bird strike at the same mass level, the drone can easily penetrate the skin and cause damages on primary structures of the aircraft. Relevant airworthiness standards should be drafted to ensure the operation safety of manned aircraft.

Acknowledgments

This report was funded by Airworthiness Certification Center of CAAC and Shanghai Aircraft Airworthiness Certification Center of CAAC. We thank Mr. Zhou Yanpei, Deputy Director of Airworthiness Certification Center of CAAC and Mr. Dai Shunan, Chief Engineer of Shanghai Aircraft Airworthiness Certification Center of CAAC for technical guidance. We thank SZ DJI Technology Co., Ltd. for supplying all the drones used in the test and related technical support.

References

[1].R. Dolbeer, S. E. Wright, J. R. Weller, A. L. Anderson, M. J. Beiger, Wildlife strikes to civil aircraft in the united states, 1990-2014, Bird Strikes.
[2].Jenkins, D, and Vasigh, B, The economic impact of unmanned aircraft systems integration in the United States, Association for Unmanned Vehicle Systems International (AUVSI), 2013, pp. 1–40.
[3].J. Ruchti, R. Senkbeil, J. Carroll, J. Dickinson, J. Holt, S. Biaz, Unmanned aerial system collision avoidance using artificial potential fields, Journal of Aerospace Information Systems 11 (3) (2014) 140–144.
[4].J. Ruchti, R. Senkbeil, J. Carroll, J. Dickinson, J. Holt, S. Biaz, Unmanned aerial system collision avoidance using artificial potential fields, Journal of Aerospace Information Systems 11 (3) (2014) 140–144.
[5].J. Asmat, B. Rhodes, J. Umansky, C. Villavicencio, Uas safety: Unmanned aerial collision avoidance system (ucas), in: IEEE Systems & Information Engineering Design Symposium, 2007, pp. 43–49.
[6].S. Georgiadis, A. J. Gunnion, R. S. Thomson, B. K. Cartwright, Bird-strike simulation for certification of the boeing 787 composite moveable trailing edge, Composite Structures 86 (1-3) (2008) 258–268.
[7].M. Guida, F. Marulo, M. Meo, S. Russo, Certification by birdstrike analysis on c27j fullscale ribless composite leading edge, International Journal of Impact Engineering 54 (2013) 105–113.
[8].C. A. S. Authority, Potential damage assessment of a mid-air collision with a small UAV, Tech. rep., Technical Report (2013).
[9].British Military Aviation Authority, "small remotely piloted aircraft systems drone midair collision study," Report-16, 2016.
[10]. Song Y, Horton B, and Bayandor J," Investigation of UAS Ingestion into High-Bypass Engines, Part 1: Bird vs. Drone," AIAA/ASCE/AHS/ASC Structures, Structural Dynamics, and Materials Conference, published online, 9-13 January 2017. doi:10.2514/6.2017-0186.
[11]. K. Schroeder, Y. Song, B. Horton, J. Bayandor, Investigation of uas in- gestion into high-bypass engines, part 2: Parametric drone study, in: 58th AIAA/ASCE/AHS/ASC Structures, Structural Dynamics, and Materials Conference, 2017, p. 0187.
[12]. Olivares G., Gomez, L., Zinzuwadia, C., Espinosa de los Monteros, J., Baldridge, R.J., and Aldag, T., "UAS Airborne Collision Severity Evaluation – Volume II – Quadcopter", Federal Aviation Administration, Report DOT/FAA/AR-XX/XX, (to be published).
[13]. Olivares G., Lacy, T., Gomez, L., Zinzuwadia, C., Espinosa de los Monteros, J., Baldridge, Aldag, T., R., Kota, K., Ricks, T., and Jayakody, N., "UAS Airborne Collision Severity Evaluation – Volume III – Fixed Wing", Federal Aviation Administration, Report DOT/FAA/AR-XX/XX, (to be published).
[14]. J. A. Reglero, M. A. Rodr´ıguez-P ́erez, E. Sol`orzano, J. A. D. Saja, Alu- minium foams as a filler for leading edges: Improvements in the mechanical behaviour under bird strike impact tests, Materials & Design 32 (2) (2011) 907–910.
[15]. J. Liu, Y. Li, X. Yu, Z. Tang, X. Gao, J. Lv, Z. Zhang, A novel design for reinforcing the aircraft tail leading edge structure against bird strike, International Journal of Impact Engineering 105 (2017) 89–101.
[16]. G. R. Johnson, A constitutive model and data for metals subjected to large strains, high strain rates and high temperatures, in: Proceedings of the 7th International Symposium on Ballistics, The Hague, Netherlands, 1983, 1983.
[17]. P. Lad ́eveze, G. Lubineau, An enhanced mesomodel for laminates based on micromechanics, Composites Science & Technology 62 (4) (2002) 533–541.
[18]. E. Sahraei, R. Hill, T. Wierzbicki, Calibration and finite element simulation of pouch lithium-ion batteries for mechanical integrity, Journal of Power Sources 201 (3) (2012) 307–321.
[19]. E. Sahraei, J. Meier, T. Wierzbicki, Characterizing and modeling mechani- cal properties and onset of short circuit forthree types of lithium-ion pouch cells, Journal of Power Sources 247 (2) (2014) 503–516.
[20]. M. A. Mccarthy, J. R. Xiao, C. T. Mccarthy, A. Kamoulakos, J. Ramos,J. P. Gallard, V. Melito, Modelling of bird strike on an aircraft wing leading edge made from fibre metal laminates c part 2: Modelling of impact with sph bird model, Applied Composite Materials 11 (5) (2004) 317–340.
[21]. S. Heimbs, Computational methods for bird strike simulations: A review, Computers & Structures 89 (23) (2011) 2093–2112.
[22]. J. Liu, Y. Li, X. Gao, Bird strike on a flat plate: Experiments and numerical simulations, International Journal of Impact Engineering 70 (4) (2014) 21–37.

[23]. S. A. Meguid, R. H. Mao, T. Y. Ng, Fe analysis of geometry effects of an artificial bird striking an aeroengine fan blade, International Journal of Impact Engineering 35 (6) (2008) 487–498.
[24]. J. Barber, J. Wilbeck, Bird impact loading, The shock and vibration bul- letin 48 (Part 2) (1978) 115–122.
[25]. M. Guida, F. Marulo, M. Meo, A. Grimaldi, G. Olivares, Sph c lagrangian study of bird impact on leading edge wing, Composite Structures 93 (3) (2011) 1060–1071.
[26]. I. Smojver, D. Ivancevic, Advanced modelling of bird strike on high lift devices using hybrid eulerian lagrangian formulation, Aerospace Science & Technology 23 (1) (2012) 224–232.